Inkjet-Printed 3D Electrode Arrays for Recording Signals from Cortical Organoids

Inola Kopic, Panagiota Dedousi, Sebastian Schmidt, Hu Peng, Oleksandr Berezin, Annika Weiße, Richard M. George, Christian Mayr, Gil G. Westmeyer, and Bernhard Wolfrum*

Monitoring electrical activity across multiple planes in 3D cell cultures and organoids is imperative to comprehensively understand their functional connections and behavior. However, traditional planar microelectrode arrays (MEAs) are intended for surface recordings and are inadequate in addressing this aspect. The limitations, such as longer production times and limited adaptability imposed by standard clean-room techniques, constrain the design possibilities for 3D electrode arrays and potentially hinder effective cell-electrode coupling. To tackle this challenge, a novel approach is presented that leverages rapid prototyping processes and additive manufacturing in combination with wet etching and electrodeposition to enhance electrode fabrication and performance. The laser-patterned MEAs on glass, polyimide (PI) foil, or polyethylene terephthalate (PET) foil substrates incorporate high-aspect ratio (up to 44:1) ink-jet printed 3D electrode structures with heights up to 1 mm at a pitch of 200 μm, enabling precise recording within cell tissues. The specific shapes of the electrode tips and customizable 3D structures provide great flexibility in electrode placement. The versatility of the 3D MEAs is demonstrated by recording the electrophysiological activity of cortical organoids in situ, paving the way for investigating neural activity under regular or various pathologically altered conditions in vitro in a high throughput manner.

1. Introduction

Various models have emerged to study the complexity of neural networks without using animal models or other living organisms. These in-vitro models have evolved from initial planar 2D cultures to multilayer 3D cultures and cell clusters, with the development of organoids being a significant milestone. Organoids consist of different types of cells and self-organize themselves to form structures resembling parts of the brain, forming vast communication networks.[1,2] One way to investigate such connectivity is by recording electrical signals via microelectrode arrays (MEAs). Typically incorporating 2D planar electrodes, MEAs have been extensively used for in-vitro studies of cell models.[3–5] Since the advent of spheroid- and organoid cultures, MEA research expanded into the 3D space to meet requirements for recording in 3D cell assemblies and tissues. Such demands for novel electrode systems have led to the development of flexible and stretchable MEAs.[6–8] Some of these structures can wrap around the organoid or act as a basket for 3D spheroids to measure signals from the outer cell layer.[9–12] Other researchers have focused on recording inside organoids using mesh-like electrodes by forming the organoid around the MEA.[13–15] While these methods have enabled signal measurement from spheroids or organoids, they have not facilitated simultaneous recording from different planes within the cell cluster nor allowed on-site device removal after

I. Kopic, P. Dedousi, H. Peng, B. Wolfrum
Neuroelectronics
Munich Institute of Biomedical Engineering
School of Computation
Information and Technology
Technical University of Munich
Hans-Piloty-Str. 1, 85748 Garching, Germany
E-mail: bernhard.wolfrum@tum.de

S. Schmidt, O. Berezin, G. G. Westmeyer
Neurobiological Engineering
Munich Institute of Biomedical Engineering
TUM School of Natural Sciences & TUM School of Medicine and Health
Boltzmannstraße 11, 85748 Garching, Germany

S. Schmidt, G. G. Westmeyer
Institute for Synthetic Biomedicine
Helmholtz Munich
85764 Neuherberg, Germany

A. Weiße, R. M. George, C. Mayr
Chair of Highly-Parallel VLSI Systems and Neuro-Microelectronics
Technical University Dresden
01062 Dresden, Germany

measurement. To meet these requirements, the use of needle-like or pillar-like MEAs has been proposed as a minimally invasive alternative.[16]

Examples of 3D MEA fabrication methods include state-of-the-art clean room processes in combination with electroplating, two-photon lithography, and modified ball bonding.[17–19] Still, there remains room for improvement, particularly concerning the fabrication of high-aspect-ratio pillars. Thus, other additive manufacturing methods have emerged as viable alternatives.[20–22] Aerosol printing has been utilized to create gold and PEDOT:PSS-based 3D microelectrode arrays, which were tested on organoids, spheroids, or in vivo in mice.[23–26] However, aerosol printing still faces limitations such as reliable scaling for high-throughput applications and cost-ineffectiveness. The additive manufacturing technique of inkjet printing presents a promising alternative, addressing these challenges effectively. We used inkjet printing in prior studies to fabricate pillar-like silver 3D microelectrodes, subsequently electroplated with platinum and gold.[27] Nevertheless, this approach lacked a process for reliable passivation of the side walls of the 3D structures, limiting specific and localized signal acquisition. Furthermore, challenges arose due to insufficient coverage of the silver structures and potential leakage of silver ions into the cellular environment.

To address these issues, we developed a streamlined process integrating inkjet printing, laser micromachining, electroplating, wet etching, and conventional cleanroom methods for fabricating highly versatile and customizable 3D MEAs. Our approach is compatible with various surfaces, from rigid glass substrates to flexible foils. It can produce high-aspect-ratio (44:1) 3D structures with customizable tip shapes and variable heights on a single chip and offers a straightforward, scalable fabrication process for experiments in multi-well plates. Here, the validation of our fabrication process involved measuring electrophysiological signals from cortical organoids directly on the chip in a rapid in situ manner, thus avoiding organoid damage and potentially enhancing throughput when combined with designs tailored for 96-well plates.

2. Results and Discussion

2.1. Fabrication of Pillar Microelectrode Arrays

The proposed fabrication process is schematically illustrated in **Figure 1A.** In general, the 3D MEAs are fabricated as follows. First, the substrate is sputtered with a thin layer of gold. This layer serves to fabricate the feedlines and electrode pads to address individual 3D pillars. The process was tested on flexible substrates (like PI or PET foil) as well as on rigid substrates like glass. An essential factor for the subsequent process steps is to ensure good adhesion between the thin metal layer and the substrate. While no adhesion layer was used for PI, the glass was pre-sputtered with titanium. Due to its sufficient roughness, PI-surfaces allow the layer to adhere mechanically, whereas, for glass, the additional layer of titanium is needed to create a sufficient bond between the thin gold layer and glass. We used a laser ablation technique for the patterning of the gold film, resulting in individually addressable electrodes, as illustrated in Figure 1B. In contrast to conventional clean-room techniques, this approach offers a rapid

and readily adaptable fabrication procedure for seamlessly integrating conductor traces with 3D structures. This step is highly customizable depending on the intended application of the MEA. In terms of dimensions, the size of the MEA is primarily constrained by the resolution of the laser on the lower end and by the dimensions of the chamber (125 mm x 125 mm) on the upper end, making it possible to create large electrode arrays as shown in Figure 1C. Regarding the substrate, the ablation process was tuned to remove thin metal films on foils, expanding the range of materials suitable for MEAs (see Figure 1D,E).

After the MEA base is formed, silver pillars are printed onto the individual electrode areas via a drop-on-demand (DOD) inkjet printing step (Figure 1A(i)). During this process, voltage pulses are applied to a piezoelectric actuator, generating pressure pulses that force droplets of silver nanoparticle ink out of the printhead nozzle and onto the substrate. Droplet over droplet is ejected onto the pad while keeping them aligned at defined locations, forming a pillar-like structure as seen in Figure 1F-H. The diameter and height of the pillar electrodes can be tuned depending on the number of droplets, the properties of the ink, and the initial droplet-to-surface interaction. Particularly, high aspect ratio pillars with an average diameter of 23 µm reaching up to ≈1 mm in height were printed in this study. This large aspect ratio of 44:1 provides high flexibility in the later connection, enabling the measurement of smaller organoids/spheroids and larger tissue slices. As a variant, the pillars can also be first printed on the metal substrate, sputtered again with gold, and subsequently processed with the laser. This variant has the advantage that potential silver leakage from the pillar shafts is reduced in case the insulation barrier should be degraded.

Another crucial aspect when measuring organoids is ensuring the ability to address several regions from precise locations. This can be achieved by insulating the pillar shaft and feedlines while exposing the pillar tip. For that, we coated the entire MEA via chemical vapor deposition (CVD) with parylene-C and opened the pillar tips using a nano-pulsed UV laser, illustrated in Figure 1A(ii),(iii). Parylene-C is mechanically robust, biocompatible, and exhibits good dielectric properties, rendering it a state-of-the-art material for biomedical applications. It acts as a support for the pillar, giving it stability, which is also significant in later steps. As mentioned before, a common challenge is to achieve sufficient adhesion between materials, specifically between the substrate or the metal and the passivation layer, as non-uniformity, underlying air bubbles, or other impurities can alter the performance of a MEA.[28]

Unlike the coating of PI or PET with parylene-C, which adheres well mechanically due to the roughness of the foil and remains durable, it is known that parylene-C tends to peel off from glass or gold surfaces, leading to an inadequate passivation layer. To prevent potential passivation failures in the future, we included an additional silanization step before applying the parylene-C coating for MEAs using glass as a substrate. After the entire chip was passivated, the tips of the 3D electrodes were opened using a perpendicular laser ablation technique (see Figure 1A(iii)).[29] This process step enables the opening of the pillar tips to achieve 3D structures with arbitrary heights. Additionally, it allows for the formation of needle-shaped openings while adjusting the heights of the pillars, all on a single MEA. **Figure 2A,B** demonstrate the diversity afforded by these steps,
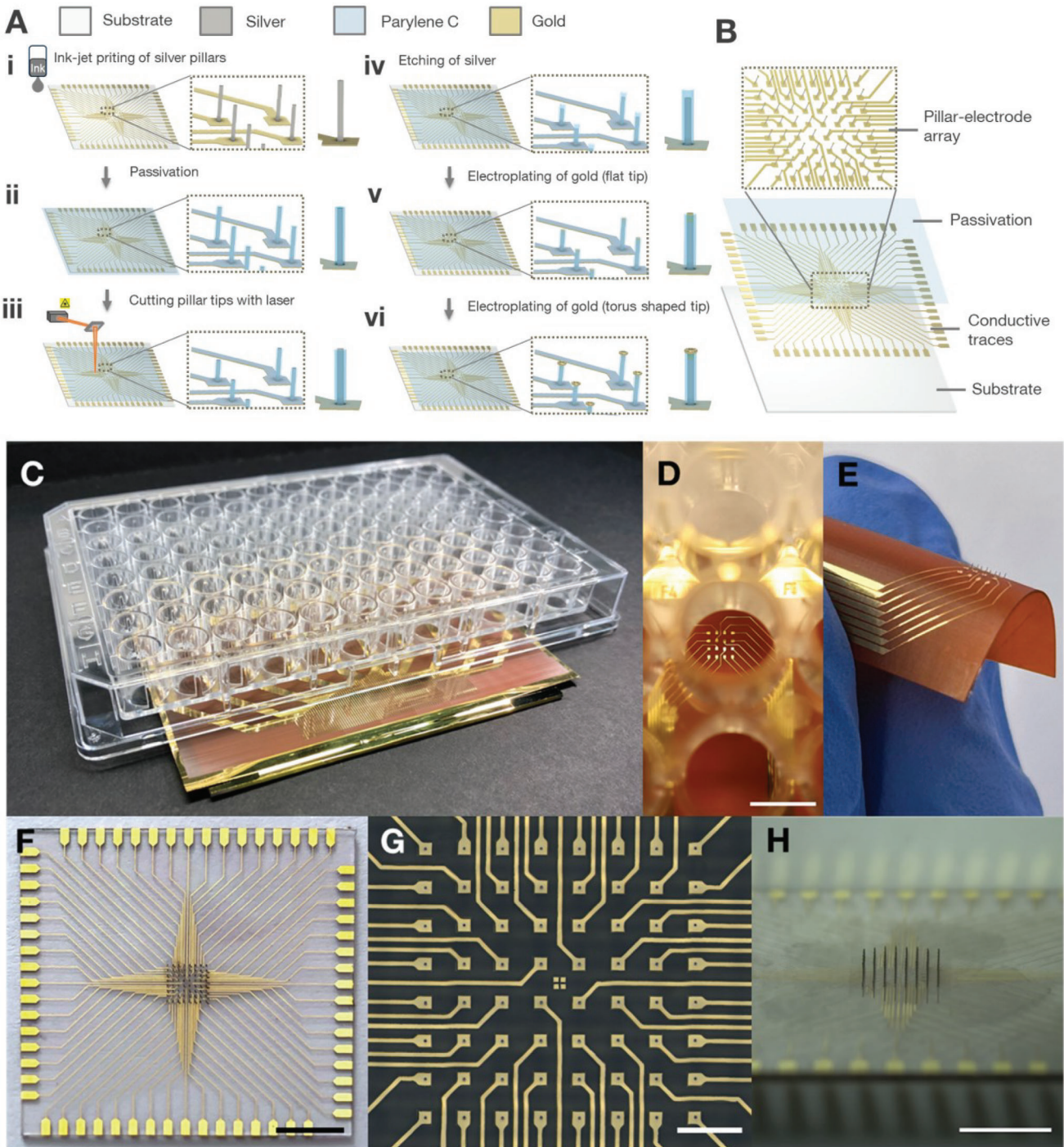
**ADVANCED
SCIENCE NEWS**

www.advancedsciencenews.com

**ADVANCED
MATERIALS
TECHNOLOGIES**

www.advmattechnol.de

Figure 1. Fabrication of 3D MEAs. A) Schematic fabrication approach for creating pillar arrays with different heights and tip shapes on a planar MEA. B) Illustration of the various layers of a 3D MEA. C) Large 3D MEA array (180 electrodes) on PI-foil integrated within a 96-well plate. D) Zoomed top-view picture on 16 pillar electrodes on PI-foil of a single well from a 96-well plate. Scale bar represents 5 mm. E) Picture of a bent 3D MEA on PI-foil with 16 pillars of 300 µm height. F) Top view picture of a gold electroplated MEA with 3D structures of 250 µm to 500 µm height and flat tips on glass. Scale bar representing 5 mm. G) Top view microscopic image of a 64-electrode array with 3D electrodes, 500 µm in height, centered on the electrode pads of a MEA with a pitch of 600 µm on PET foil. Scale bar indicating 1 mm. H) Zoomed side view of a 3D MEA on the 64-pillar array with a uniform height of 650 µm. Scale bar corresponding to 5 mm.
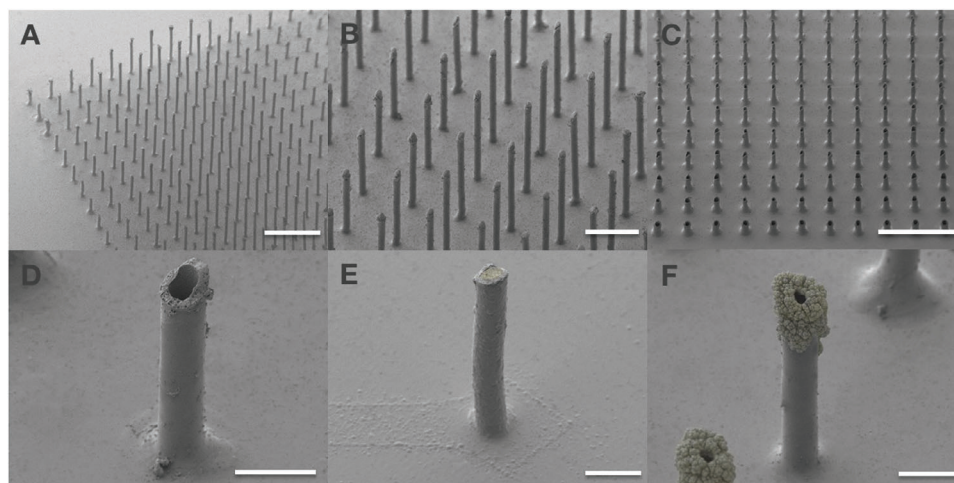
**ADVANCED
SCIENCE NEWS**

www.advancedsciencenews.com

**ADVANCED
MATERIALS
TECHNOLOGIES**

www.advmattechnol.de

Figure 2. SEM images of 3D MEAs and individual pillars. SEM image of A) a pillar array with 256 needles and various heights, B) a zoomed-in view of needle-shaped pillars, C) a tube-pillar array with a height of 150 ± 9 μm after silver etching, D) an individual etched pillar with 120 μm in height, E) an individual pillar after gold electroplating at −1.15 V with a height of 240 μm, F) an individual pillar after gold electroplating at −1.5 V, with height of 145 μm. Gold metal structures are indicated by the colored areas (E,F). All SEM images were acquired using electron beam acceleration voltage of 3 kV. The scale bars shown have a length of 500 μm, 200 μm, 500 μm, 50 μm, 100 μm and 50 μm (A-F), respectively. The galvanization potential was applied versus a Ag/AgCl reference electrode.

showing the range of resulting possibilities in terms of pillar tip shape (flat or needle-shaped) and height variation.

A major disadvantage of using silver as the conductive metal for MEAs is its cytotoxic effect on cells.[30] To enhance cell viability for long-term measurements, we employed a combination of wet etching of portions of the silver pillar and electrodeposition of gold. Therefore, we used a mixture of hydrogen peroxide and ammonia to back-etch the silver core from the tip of the pillar structure, following the chemical reaction:

$$2Ag + 4NH_3 + H_2O_2 \rightarrow 2Ag(NH_3)_2^+ + 2OH^- \qquad (1)$$

Hydrogen peroxide, an oxidizing agent, ensured controlled dissolution of Ag and uniform etching due to its stabilizing properties. The base (ammonia) can form soluble complexes with Ag ions, enhancing their solubility and removal, thus promoting the efficacy of Ag oxide dissolution. With this relatively fast process, tubular structures, as illustrated in Figure 1A(iv) and shown in Figure 2C,D, were generated. The passivated parylene-C shafts act as a guide for the liquid and keep the 3D structure intact. In the final step, the individual pillars were electroplated with gold (see Figure 1A(v-vi)). This coating aimed to ensuring both biocompatibility and low impedance. We employed pulsed electrodeposition (PED) involving a duty cycle for metal deposition and a reversed cycle for ion recovery. This ensures a smoother gold deposition by removing impurities on the surface and entrapped hydrogen. We used different deposition protocols with reduction potentials of −1.15 V versus Ag/AgCl or −1.5 V versus Ag/AgCl, as described in the experimental section. All proposed electroplating variants resulted in gold deposition, where the shape can be changed from a flat tip to a torus-shaped tip depending on the applied voltage, as shown in Figure 2E,F. To prepare and evaluate the performance of the 3D MEAs, the pillars were optically and electrochemically characterized before and after electroplating.

2.2. Characterization of Pillar Microelectrode Arrays

To evaluate the quality of passivation, stability testing was conducted using chronoamperometry (CA), where a constant voltage is applied to induce hydrogen reduction on the electrodes, forming bubbles at the openings. The detailed protocol is provided in the Experimental Section/Methods-Section. This method enables the detection of possible pinholes along the feedlines, indicating insufficient passivation. The parylene-C coating exhibited stability, with no pinholes observed on the feedlines and electrolysis only appearing at the laser-ablated pillar openings, indicating sufficient adhesion of the passivation layer.

We assessed the etching rate within the pillar structure (**Figure 3A(ii)**) by measuring the height of the silver cores at different time points after exposure to the etching solution. The resulting etching depths were 31.0 ± 2.0, 42.5 ± 1.9, 51.7 ± 1.7, and 60.0 ± 1.9 μm after 2.5, 5, 7.5, and 10 min, respectively (mean and standard deviation $n_{2.5\,min}$ = 31, $n_{5\,min}$ = 22, $n_{7.5\,min}$ = 24, $n_{10\,min}$ = 22) as shown Figure 3B. The average diameter of the needle openings was 23.1 ± 2.1 μm ($n_{diameter}$ = 54). As expected, the etching depth increased over time due to the oxidation of silver metal to silver ions in the H_2O_2:NH_3 solution, and the etching rate decreased with increasing depth of the hollow needle structure.

To investigate the gold electroplating processes, the effect of the reduction voltage (−1.15 V versus −1.5 V), the effective electroplating time (25 ms versus 50 ms), and the number of cycles (600 versus 1800 versus 2400) were investigated. Using a reduction potential of −1.15 V and a duty cycle of 25 % and 50% against a Ag/AgCl (3 M NaCl) reference electrode, the pillar tubes were filled with gold after ≈600 cycles, as seen in Figure 2E and Figure 3A(iii), resulting in a flat tip. Similar results with cycle numbers of 1800 and 2400 indicated a self-limiting deposition process. For deposition potentials of −1.5 V, we observed an increase in gold deposition with increasing cycle numbers,
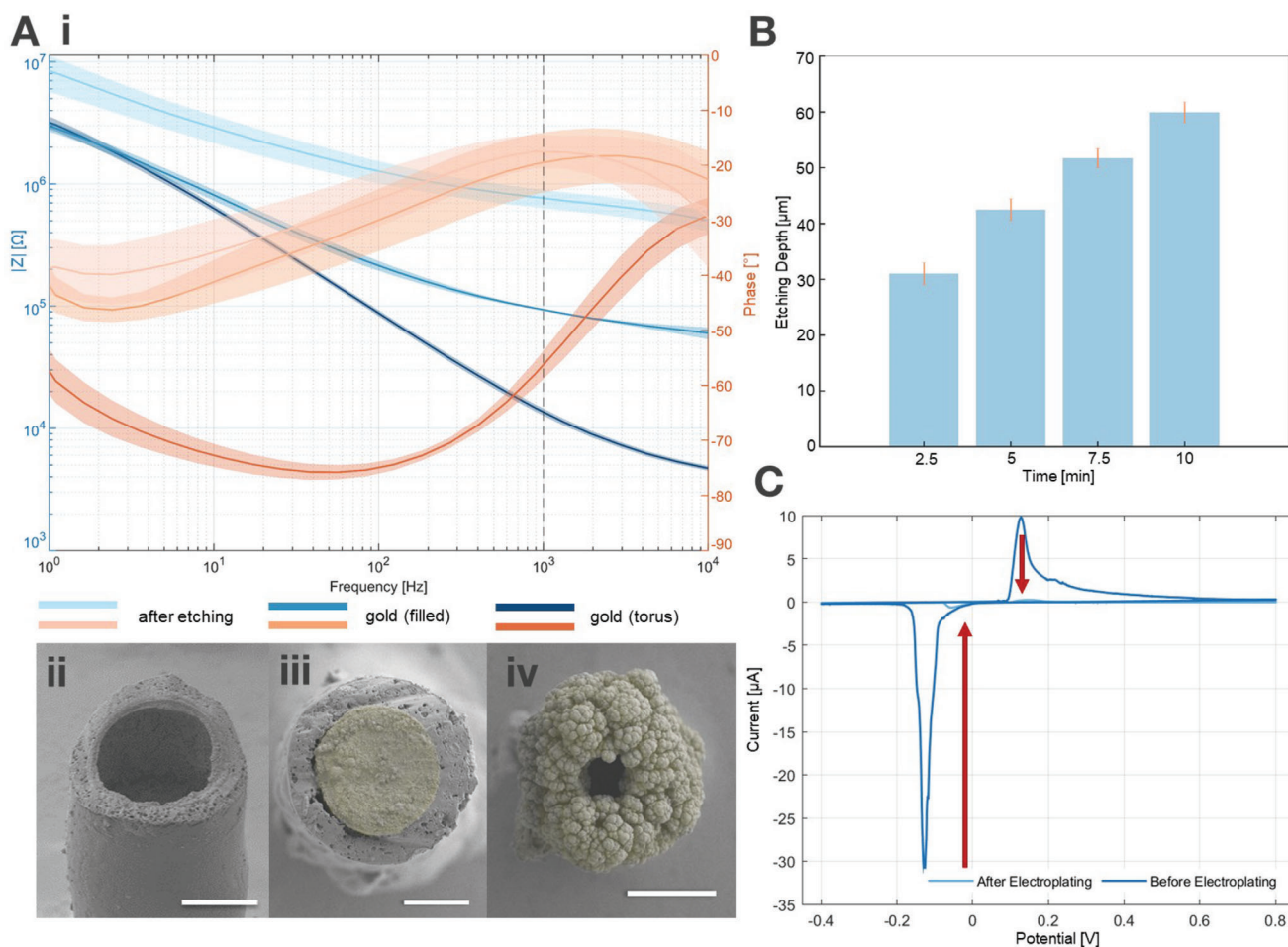
2400645 (4 of 9)

**ADVANCED
SCIENCE NEWS**

www.advancedsciencenews.com

**ADVANCED
MATERIALS
TECHNOLOGIES**

www.advmattechnol.de

Figure 3. Electrochemical and optical characterization of 3D pillar electrodes after etching and after Au-electrodeposition. A) (i) Magnitude and phase of the impedance of 3D pillars before and after Au-electroplating with −1.15 V and −1.5 V versus a Ag/AgCl reference electrode, respectively. The mean and standard deviation (solid line and shaded area, respectively) were calculated using 20 samples. A (ii-iv) SEM images of the tip 3D pillars after etching (ii), after electroplating with −1.15 V (iii), and after electroplating with −1.5 V (iv). The colored area indicates gold (iii-iv). All SEM images used an acceleration voltage of 3 kV. The scale bars shown have a length of 20 µm, 10 µm, and 20 µm (ii-iv), respectively. B) Bar plot of the tube depth of 3D pillars after silver etching for 2.5, 5, 7.5, and 10 min with the standard deviation calculated across $n_{2.5\,min} = 31$, $n_{5\,min} = 22$, $n_{7.5\,min} = 24$, $n_{10\,min} = 22$ samples, respectively. C) Example cyclic voltammetry, i.e., current plotted against the potential at the working electrode, for a single pillar before etching and after gold deposition, swept from −0.4 to 0.8 V, with a scan rate of 50 mVs^{-1}. All potentials were measured against a Ag/AgCl reference electrode. The red arrows indicate the reduction of the silver peaks in Au-electroplated samples.

resulting in torus-shaped electrodes (see Figure 2F and Figure 3A(iv)). At this highly negative potential, other side reactions, such as the reduction of water to hydrogen gas, became predominant, leading to irregular nucleation and an overgrowth of gold beyond the passivation, whereas, at −1.15 V, the deposition resulted in a smooth and homogenous surface. Increasing the effective deposition time or duty cycle decreased the total process time by 30%, achieving similar results without a prominent loss in quality.

To characterize the electroplated 3D electrodes, we performed cyclic voltammetry (CV) in electrolyte solution (PBS). To evaluate the quality of the electroplating process and specifically whether the silver was completely covered, the cyclic response for single silver and gold-plated 3D pillars in PBS from −0.4 to 0.8 V with a scan rate of 50 mV s^{-1} was compared, as shown in the Figure 3C. Silver oxidation and reduction peaks typical for silver

are observed in PBS at 126 ± 3 mV and −127 ± 3 mV versus Ag/AgCl (3 M NaCl), respectively. Upon examining the cyclic response of a gold electrode, it is evident from the CV that the silver oxidation peak was substantially reduced from an amplitude of 9.7 µA to 0.02 µA for both flat gold tips and torus-shaped gold pillars. This demonstrates the successful gold deposition within the etched parylene tubes.

To further investigate the electrochemical properties of individual pillars before and after etching, as well as after electroplating, electrical impedance spectroscopy (EIS) in PBS was performed. To this end, a low-amplitude sinusoidal signal with 10 mV amplitude from 1 Hz to 10 kHz was applied.

The impedance magnitude and phase before and after silver etching showed a similar impedance profile, indicating that the electrode-electrolyte interface remained stable and the area remained approximately constant. Figure 3A(i) displays the mean
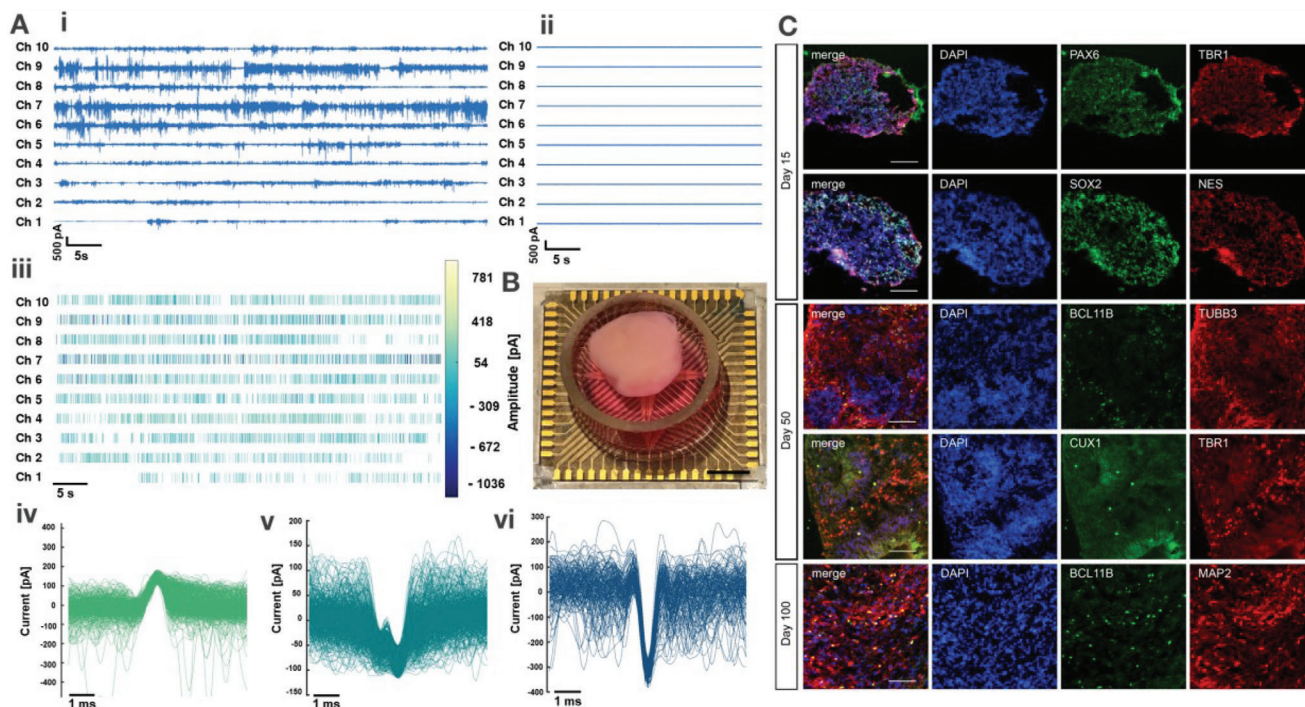
Figure 4. 3D MEA recording on hiPSC-derived cortical organoids. A) time traces of signals recorded with an organoid (i) and without an organoid (ii). Each channel corresponds to a single Au-electroplated pillar with a flat tip with an average height of 250 ± 3 µm of a 3D MEA. (iii) Amplitude and temporal occurrence of spikes with a minimum threshold of 50 pA detected from the time traces (i) and overlapping shapes of the average recorded spikes in the traces (n = 631 (iv), n = 543 (v), n = 175 (vi)). B) Picture of a neuronal organoid (534 days in vitro) on top of a 3D MEA with Au-electroplated flat pillar tips with an average height of 250 ± 2 µm in media. The scale bar shown has a length of 5 mm. C) Fluorescence microscopy images of the immunofluorescence (PAX6, SOX2, BCL 118, CUX1 green; TBR1, NES, TUBB3, MAP2, red; and DAPI, blue) in a 40 µm thick section of a cortical organoid after 15, 50, and 100 days of differentiation, respectively. The scale bar in all images corresponds to 100 µm.

impedance of individual silver pillars before and after etching (n = 15), after electrodeposition of a flat gold tip pillar (n = 15), and after electrodeposition of a torus-shaped pillar (n = 15). The depicted impedance magnitudes follow a characteristic trace typical for Ag and Au 3D microelectrodes.[31] Specifically, the impedance at 1 kHz was measured to be 731 ± 62 kΩ for recessed silver-core pillars after etching, 87.3 ± 1.3 kΩ for flat gold-core pillars, and 11.3 ± 1.5 kΩ for torus pillars. As expected, the electroplated torus-shaped gold pillar electrodes exhibit the lowest impedance of all electrodes. This can be attributed to the larger surface area of gold for torus-shaped tips compared to flat tips.

2.3. Pillar MEA Recording and Stimulation of hiPSC-Derived Cortical Organoids

We demonstrated the applicability of the 3D MEAs to measure the activity of cortical brain organoids using a custom-built amperometric amplifier system.[32] To generate the cortical organoids, we used a protocol that mimics the architecture of the embryonic human cerebral cortex during its development.[33] On Day 15, the majority of cells within the neural-tube-like structures were positive for the neuronal precursor cell (NPC) markers SOX2 and NES, or the intermediate progenitor cell marker TBR1, as well as the dorsal forebrain NPC marker PAX6 (**Figure** 4C). These neural-tube-like structures developed independently into cortical structures organized into distinct layers, as shown by the

distribution of intermediate progenitor cells (TBR1) and neurons of the upper (CUX1) or lower cortical layers (BCL11B) at day 50 (Figure 4C). These developmental layers diminished during the further differentiation process, resulting in an even distribution of cortical neurons within the fully differentiated organoid, as shown at day 100 (Figure 4C). Afterward, the organoids no longer underwent any structural changes. Instead, the neurons matured with no additional structural changes and formed neuronal networks with spontaneous activity patterns.

After reaching full maturation, organoids of various sizes (ranging from 300 µm up to 9 mm in diameter) were placed into the wells of the MEAs, which had pillar heights of 150 – 250 µm and were electroplated with gold at −1.15 V, as shown in Figure 4B. Prior to testing, a glass ring was glued onto the MEAs to keep the organoid in media during measurements. Amperometric recordings were performed using a custom-built amplifier system. The extracellular readout signals were filtered with a 60 Hz high-pass and a 1200 Hz low-pass filter to better distinguish the spontaneous bursts of electrical activity. Spontaneous burst activity was recorded from cortical organoids. Typical traces are plotted in Figure 4A(i) (working electrodes n = 44, signals from 45% of channels during one recording). To verify whether signals were originating from neurons, negative control recordings were performed on the same chip without the organoids (Figure 4A(ii)). These experiments revealed no characteristic signals and displayed an average noise level of 18.3 ± 3.6 pA per channel (n = 62). For spike detection, a threshold of 50 pA was

ADVANCED
SCIENCE NEWS

www.advancedsciencenews.com

ADVANCED
MATERIALS
TECHNOLOGIES

www.advmattechnol.de

used, and the temporal occurrence and amplitude of the spikes are displayed in Figure 4A(iii). The average peak-to-peak amplitude across all channels was 219 ± 156 pA, with signal-to-noise ratios (SNRs) up to 49.5 ± 6.1.

The organoids exhibit their characteristic bursting signals occurring in clusters. This observation aligns with previous literature, which suggests that as organoids mature, they tend to display more bursting activity.[34] Additionally, our analysis revealed different spike shapes, as depicted in Figure 4A(iv-vi). Short-duration, high-amplitude spikes originate from single neurons, while slower signals with lower amplitudes indicate compound recordings involving multiple neurons.

The variability in spike amplitudes can be attributed to variations in the activity levels of different areas within the organoid. Moreover, the electrode spacing of the MEAs plays a crucial role in cellular recordings. While large electrode spacing can cover a broad area within the organoid, it may not effectively capture signal propagation. Since we used an electrode spacing of 600 μm in our experiments to cover a large area of the organoid, this setup may not effectively capture signal propagation, resulting in no distinct observation of synchronized activity between different channels despite the advanced maturation age of the organoids. Furthermore, differential nutrient levels exist within an organoid, with nutrient availability decreasing toward the core. Consequently, a necrotic core is common for these organoids upon reaching a specific size, leading to lower or non-prominent recorded signal amplitudes.[35]

To further study the synchrony of neural activities in cortical organoids, the spacing of the electrodes of each MEA can be reduced, and the electrode number increased to ensure that a broad area is addressed while measuring the cellular response across individual pillars. Additionally, the nourishment of organoids can be optimized by using microfluidics to maintain the core of the organoid and improve the medium for electrophysiological measurements.

3. Conclusion

We have developed a fabrication method for producing arrays of high-aspect-ratio (44:1) 3D pillar electrodes using a combination of ink-jet printing, laser micromachining, wet etching, and electrodeposition techniques. This approach enables the fabrication of arrays with varying electrode heights and tip shapes, including sharp, needle-like, and toroidal geometries. Our 3D MEAs have been successfully utilized for electrophysiological signal recordings on cortical organoids derived from hiPSCs, resulting in improved signal quality and enhanced cell-electrode coupling. We anticipate that this approach will advance the field of 3D cell cultures and organoid electrophysiology, facilitating more profound insights into complex biological systems and enabling the development of targeted therapeutic interventions in a customized yet high-throughput manner. From a future perspective, our device could be used for long-term measurements to study the effects of various drugs on tissues in vitro.

4. Experimental Section

Materials: penicillin/streptomycin, Dulbeccos's phosphate saline (PBS 1x), 3-(trimethoxysilyl)propyl methacrylate (silane1, > 98%), (3-

Mercaptopropyl)trimethoxysilane (silane2, 95%), cAMP, formalin (F5554, 10%), sucrose (S0389, 30%), PBS containing 1% BSA, Triton X-100 (0.3%), DAPI, CUX1 (SAB1405681) and TUBB3 (T5076) were acquired from Sigma-Aldrich (USA). Ethidium homodimer-1, Geltrex Matrix, collagenase IV, low attachment 6-well plates, NES (Ma1110), donkey-anti-goat IgG Alexa 488 (A11055), donkey-anti-mouse IgG Alexa 488 (A21202), donkey-anti-mouse IgG Alexa 594 (A21203), donkey-anti-rabbit IgG Alexa 594 (A21207) and donkey-anti-rat IgG Alexa 488 (A21208) were bought from ThermoFisher Scientific (USA). Polydimethylsiloxane (PDMS Sylgard 184 (10:1 w/s base/curing agent)) and Matrigel Matrix were purchased from Dow Corning (USA). 2-Propanol (99.5%) (IPA), ethanol (99.5%) and L-ascorbic acid were purchased from Carl Roth (Germany). The Silane-A174 adhesion promoter was purchased from Plasma Parylene Systems GmbH (Germany). Deionized water was taken from Ultra Clear purification system/Berry Tec (Germany). Ammonia solution (28%) and hydrogen peroxide (31%) were purchased from VLSI Selectipur, BASF SE (Germany). StemMACS iPS-Brew XF (human), dorsomorphin, SHH, SB 431 542, BDNF, and GDNF were purchased from Milteyni Biotec (Germany). 20% Knockout serum replacement, GlutaMAX, NEAA, 2-Mercaptoethanol, DMEM/F12 (11330-032), N2 supplement, B27, and Neurobasal medium were bought from Life Technologies (USA). A-83 and CHIR 99 021 were acquired from Tocris Bioscience (United Kingdom). Neg-50 (6502) was obtained from Epredia (Germany) and Aqua-Poly/Mount from Polysciences Inc. (USA). PAX6 (ab78545), TBR1 (ab31940), BCL11B (ab18465), MAP2 (ab5392) were purchased from Abcam (United Kingdom).

SOX2 (sc17320) was acquired from Santa Cruz Biotechnology (USA) and goat-anti-chicken IgG Alexa 594 (103-587-008) from Dianova (Germany).

Electrode Fabrication: First, sample substrates ($24 \times 24 \times 0.5$ mm^3 glass slides (Matsunami Glass, Japan), $100 \times 100 \times 0.125$ mm^3 PI-foils (CMC Klebetechnik GmbH, Germany), $100 \times 100 \times 0.125$ mm^3 Ti-Wolfram/Au (20 nm/100 nm) sputtered PET-foils) were sonicated (Bransonic ultrasonic cleaner 5510E-MTH, Branson ultrasonics, USA) for 15 min in acetone, IPA and deionized water, respectively. A layer stack of 25 nm Ti and 200 nm of Au (5×10^{-3} mbar argon, 12 W Au, 40 W Ti, Moorfield nanoPVD, UK) was sputtered on the glass slides, while PI-foils were sputtered with 150 nm of gold (30 mA, 8×10^{-3} mbar, Bal-tec MED 020, Lichtenstein).

3D pillars were printed on the samples using a silver nanoparticle ink (Silverjet DGP 40LT-15C, Sigma-Aldrich, USA) with a state-of-the-art inkjet printer (CeraPrinter F-Series, Ceradrop, France). Before printing, the Ag nanoparticle ink was sonicated (Bransonic ultrasonic cleaner 5510E-MTH, Branson ultrasonics, USA) for 30 min, filtered using a poly(vinylidene fluoride) filter (GD/X, Whatman, Maidstone, UK; pore size: 0.2 μm), and loaded into a disposable 2.4 pL cartridge (Samba, Fujifilm Dimatix, USA). To eject individual droplets, a voltage pulse of 40 V with a rise, dwell, and falling time of 3, 12, and 1 μs was applied. The nozzle plate and the sample stage were held at 45 and 50 °C, respectively. The 3D pillars were printed using a moving print head with a speed of 72 mm s^{-1} with a drop-to-drop interval of 120 Hz and a number of droplets of 500 to 1500. Depositing 500 droplets results in a pillar height of 216 ± 6 μm (n = 30). Here, across 6 samples, 5 pillars were measured, respectively. The printing process for two complete MEAs takes approximately 3 hours of unsupervised printing time. Once printed, the Ag-pillar arrays were thermally sintered in an oven for 2 h at 150 °C.

Filled areas and boundaries of the layout on glass (fill: 45% power, 500 mm s^{-1} speed, 70 kHz frequency, 2 repetitions, 0.015 mm fill interval, contour pattern; boundary: 2% power, 500 mm s^{-1} speed, 70 kHz frequency, 1 repetition), PI-foil (1st fill: 15% power, 400 mm s^{-1} speed, 60 kHz frequency, 1 repetition, 0.015 mm fill interval, slant pattern; 2nd fill: 15% power, 400 mm s^{-1} speed, 60 kHz frequency, 1 repetition, 0.015 mm fill interval, 90° angle, slant pattern; boundary: 4% power, 400 mm s^{-1} speed, 60 kHz frequency, 1 repetition) and PET-foil (fill: 15% power, 400 mm s^{-1} speed, 60 kHz frequency, 2 repetitions, 0.015 mm fill interval, contour pattern; boundary: 2% power, 400 mm s^{-1} speed, 60 kHz frequency, 1 repetition) were patterned and both foils additionally cut into 24.15×24.15 mm^2 squares (100% power, 1000 mm s^{-1} speed, 40 kHz

frequency, 80 repetitions) by a nanosecond pulsed laser scanner (MD-U1000, Keyence, Japan). Afterwards, all samples were rinsed with IPA and deionized water.

To improve the adhesion between the substrate and the passivation, glass, PI, and PET surfaces were O_2 plasma treated (0.8 mbar, 80% power, 5 min, Diener Femto Asher, Diener Electronic, Germany). Additionally, glass substrates underwent a vapor-phase silanization procedure, where the samples were placed together with a silane1-IPA-solution (20, 80 wt.%) and a silane2-IPA-solution (20, 80 wt.%) at 100 °C for 2 h in an oven, rinsed thoroughly with IPA and dried at 120 °C for 1 hour, respectively. A 5 μm-thick parylene-C layer was deposited via chemical vapor deposition (SCS Labcoter 2, PDS 2010, Specialty Coating Systems, USA) from 3.15 g of dimer precursor (Daisan Kasei, Japan). For PI- and PET-samples 200 μL of the adhesion promoter Silane A-174 was added in the deposition chamber. The electrode pads of all samples were covered with PDMS strips before parylene-C deposition.

The following step included cutting the electrode tips open with the MD-U1000C marking laser using 100% power, 500 mm s^{-1} speed, 40 kHz frequency, and 100 repetitions. Therefore, the samples were positioned on a vacuum chuck, and the pillars were oriented perpendicular to the laser beam. Next, the MEAs were placed in the etching mixture of hydrogen peroxide and ammonia solution (50, 50 wt.%) for 2.5, 5, 7.5, and 10 min to remove the silver from the exposed pillars down to the desired depth, respectively.

Finally, gold was electroplated on the tubular pillars to inhibit silver leakage into the medium during organoid experiments. To contain the electrolyte, glass rings (height, outer diameter, and inner diameter of 15, 17, and 14.6 mm, respectively) were dipped into degassed PDMS, placed on top of the MEA and then cured for 1 h at 100 °C in an oven.

An aqueous potassium gold cyanide bath (KAu[CN]$_2$, Pur-A-Gold 401B, Enthone-OMI, Netherlands) was used as the electrolyte. CA was then employed in a three-electrode setup to deposit gold using a potentiostat (VSP-300, Bio-Logic Science Instruments, France). Specifically, the etched 3D pillars acted as the working electrode, a larger platinum mesh as the counter electrode, and a Ag/AgCl electrode (3 M NaCl, BASI, United Kingdom) as the reference. The reduction potential for KAu[CN]$_2$ was set to −1.15 V and −1.5 V versus Ag/AgCl to generate a filled tube and a torus-shaped tip, respectively. For a controlled deposition, 25 ms effective deposition was favored over 50 ms effective deposition, followed by a resting interval of 75 ms and 50 ms of 0.3 V, respectively.

Depending on the depth of the tubes and the amount of gold to be electrodeposited, 600, 1800, or 2400 cycles were used. Lastly, all samples were rinsed with deionized water and IPA, dried in an oven at 70 °C for 1 h, and stored until further usage at room temperature.

Imaging: A 3D laser scanning confocal microscope (VK-X250, Keyence, Japan) with a 100X objective was used to image the electrodes before and after etching. The images were analyzed with the software MultiFile Analyzer (Keyence, Japan) and the etched depth was calculated. For the SEM images, the samples were first sputtered with 15 nm of gold (30 mA, 8×10^{-3} mbar, Bal-tec MED 020, Lichtenstein). The samples were fixed on SEM specimen stubs with a conductive double-sided carbon pad and afterwards imaged with a scanning electron microscope (Gemini 2, Zeiss Crossbeam 550, Germany) using a SE2 detector and a beam current of 1 nA. The obtained images were processed in GIMP.

Electrochemical Characterization: Chronoamperometry, cyclic voltammetry, and impedance spectroscopy were performed in PBS using a potentiostat (VSP-300, BioLogic Science Instruments, France) in a three-electrode setup with a Ag/AgCl (3 M NaCl, BASI, United Kingdom) reference electrode, a platinum coil wire as counter electrode and individual pillars as working electrode. CA was conducted at −2 V for 30 s to assess the stability of the passivation. The CV measurements were performed between −0.4 V and 0.8 V with a scan rate of 50 mV s^{-1} for 6 cycles. Impedance spectroscopy recordings were conducted by applying a sinusoidal signal with 10 mV amplitude at 0 V and frequencies from 1 Hz to 10 kHz.

Cortical Organoids: Cortical organoids were differentiated according to a protocol published by Qian et al. 2018.[33] In brief, human induced pluripotent stem cells (hiPSCs) (ISFi001-A-RRID: CVCL_YT30) were main-

tained on Geltrex coating and in human iPS-Brew XF at 37 °C, 7% CO$_2$ and 21% O$_2$. If not indicated otherwise, the medium was changed daily. Upon reaching a colony size of ≈1.5 mm, colonies were detached using a 2 mg mL^{-1} collagenase IV solution for 45 – 60 min and incubated in iPS-Brew XF medium for 24 h in low-attachment 6-well plates on a 3D-Rocker/shaker at 37 °C, 5% CO$_2$ and 21% O$_2$. The next day, the medium was replaced by the first forebrain specific medium [20% Knockout serum replacement, 1 x GlutaMAX, 1 x NEAA, 0.02% 2-mercaptoethanol, 1 x penicillin-streptomycin, 2 μM dorsomorphin, 2 μM A-83, 100 ng mL^{-1} SHH in DMEM/F12]. At days 5, medium was replaced by the second forebrain specific medium [1 x N2 supplement, 1 x GlutaMAX, 1 x NEAA, 1 x penicillin-streptomycin, 1 μM CHIR, 1 μM SB 431542 in DMEM/F12]. At day 7, the formed embryoid bodies (EBs) were embedded in Matrigel and cultivated in the Matrigel "cookie" for 5 days in the second forebrain-specific medium at 37 °C, 5% CO$_2$, and 21% O$_2$, but not on the 3D-Rocker/shaker. On day 14, organoids were released from the cookie using a 5 ml pipette tip. The medium was replaced by the third forebrain-specific medium [1 x N2 supplement, 1 x B27, 1 x GlutaMAX, 1 x NEAA, 1 x penicillin-streptomycin in DMEM/F12]. Organoids were transferred into a low-attachment 6-well plate and incubated on a 3D-Rocker/shaker at 37 °C, 5% CO$_2$, and 21% O$_2$ with medium changes every third day. On day 35, Matrigel (1:100) was added to the third forebrain-specific medium. At day 70, medium was changed to the fourth forebrain-specific medium [1 x B27 supplement, 1 x GlutaMAX, 1 x NEAA, 1 x penicillin-streptomycin, 200 μM L-ascorbic acid, 500 μM cAMP, 20 ng mL^{-1} BDNF, 20 ng mL^{-1} GDNF in Neurobasal medium] with medium changes every fourth day.

Fluorescence Imaging: At the indicated differentiation stage, organoids were collected, maintenance medium was removed, organoids were washed once with PBS, and fixed in 10% formalin for 20 min at 4 °C. After fixation, the organoids were washed thrice with PBS and incubated in a 30% (w/v) sucrose cryoprotectant solution until fully saturated. The next day, organoids were transferred into a small "embedding form" (7 mm x 7 mm) and distributed (if multiple organoids were embedded per form). The form was filled with Neg-50 freezing medium and stored at −80 °C until they were sectioned at −20 °C into 40 μm thick horizontal sections using a freezing cryostat and mounted on slides.

Immunostainings: Immunostainings were performed as described in a prior study.[36] The sections were thawed at room temperature for 15 min. Blocking and permeabilization were performed using a blocking solution [PBS containing 1% BSA and 0.3% Triton X-100] for 1 h at room temperature. Primary antibodies were diluted in blocking solution, and antibody incubation was performed at 4 °C overnight. Sections were washed twice with PBS and incubated with secondary antibodies diluted in blocking solution for 2 h at room temperature. Nuclei were stained using a 0.1 μg mL^{-1} DAPI-PBS solution for 10 min at room temperature. Sections were washed thrice with PBS, and coverslips were mounted using Aqua-Poly/Mount.

Primary antibodies were diluted as follows: CUX1 (1:1000), TUBB3 (1:500), PAX6 (1:500), TBR1 (1:500), SOX2 (1:500), NES (1:250), BCL11B (1:1000), MAP2 (1:500). Secondary antibodies were diluted as follows: donkey-anti-goat IgG Alexa 488 (1:500), donkey-anti-mouse IgG Alexa 488 (1:500), donkey-anti-mouse IgG Alexa 594 (1:500), donkey-anti-rabbit IgG Alexa 594 (1:500), donkey-anti-rat IgG Alexa 488 (1:500), goat-anti-chicken IgG Alexa 594 (1:500).

Extracellular Recordings and Electrical Stimulation: Prior to organoid placement, the 3D-pillar MEAs were sterilized by immersing them in ethanol for 2 hours and drying them overnight under the cell bench. The organoids (age: 20 months) were gently placed in the wells on top of the 3D-pillars of the MEAs using a cell strainer, and a fresh medium (DMEM/F12) was added. Extracellular signals were recorded amperometrically using an in-house built 64-channel amplifier shielded in a Faraday cage. The amplifier features a 10 kHz sampling rate and a 1 GΩ feedback resistor. The recordings were conducted using a Ag/AgCl reference electrode. First, the spontaneous activity of cortical organoids was recorded for 5 to 10 min. After recordings, the organoids were transferred back to the low-attachment 6-well plate. The pillar MEAs were rinsed with PBS, fresh media was added to the well of the MEAs, and negative control measurements were performed on the used MEAs. Altogether, the measurements

lasted approximately 45 to 60 min. The data analysis was conducted in MATLAB (MathWorks, USA).

Conflict of Interest

The authors declare no conflict of interest.

Data Availability Statement

The data that support the findings of this study are available from the corresponding author upon reasonable request.

[1] J. A. Brassard, M. P. Lutolf, *Cell Stem Cell* **2019**, *24*, 860.

[2] O. L. Eichmüller, J. A. Knoblich, *Nat. Rev. Neurol.* **2022**, *18*, 661.

[3] A. Czeschik, P. Rinklin, U. Derra, S. Ullmann, P. Holik, S. Steltenkamp, A. Offenhäusser, B. Wolfrum, *Nanoscale* **2015**, *7*, 9275.

[4] X. Dai, W. Zhou, T. Gao, J. Liu, C. M. Lieber, *Nature Nanotech* **2016**, *11*, 776.

[5] W. G. Regehr, J. Pine, C. S. Cohan, M. D. Mischke, D. W. Tank, *J. Neurosci. Methods* **1989**, *30*, 91.

[6] D. A. Soscia, D. Lam, A. C. Tooker, H. A. Enright, M. Triplett, P. Karande, S. K. G. Peters, A. P. Sales, E. K. Wheeler, N. O. Fischer, *Lab Chip* **2020**, *20*, 901.

[7] J. Y. Lee, S. H. Park, Y. Kim, Y. U. Cho, J. Park, J.-H. Hong, K. Kim, J. Shin, J. E. Ju, I. S. Min, M. Sang, H. Shin, U.-J. Jeong, Y. Gao, B. Li, A. Zhumbayeva, K. Y. Kim, E.-B. Hong, M.-H. Nam, H. Jeon, Y. Jung, H. Cheng, I.-J. Cho, K. J. Yu, *npj Flex Electron* **2022**, *6*, 86.

[8] V. Rincón Montes, J. Gehlen, S. Ingebrandt, W. Mokwa, P. Walter, F. Müller, A. Offenhäusser, *Sci. Rep.* **2020**, *10*, 19836.

[9] Q. Huang, B. Tang, J. C. Romero, Y. Yang, S. K. Elsayed, G. Pahapale, T.-J. Lee, I. E. Morales Pantoja, M. Pantoja, F. Han, C. Berlinicke, T. Xiang, M. Solazzo, T. Hartung, Z. Qin, B. S. Caffo, L. Smirnova, D. H. Gracias, *Sci. Adv.* **2022**, *8*, eabq5031.

[10] T. L. Li, Y. Liu, C. Forro, X. Yang, L. Beker, Z. Bao, B. Cui, S. P. Paşca, *Biomater.* **2022**, *290*, 121825.

[11] A. Kalmykov, C. Huang, J. Bliley, D. Shiwarski, J. Tashman, A. Abdullah, S. K. Rastogi, S. Shukla, E. Mataev, A. W. Feinberg, K. J. Hsia, T. Cohen-Karni, *Sci. Adv.* **2019**, *5*, eaax0729.

[12] Y. Park, C. K. Franz, H. Ryu, H. Luan, K. Y. Cotton, J. U. Kim, T. S. Chung, S. Zhao, A. Vazquez-Guardado, D. S. Yang, K. Li, R. Avila, J. K. Phillips, M. J. Quezada, H. Jang, S. S. Kwak, S. M. Won, K. Kwon, H. Jeong, A. J. Bandodkar, M. Han, H. Zhao, G. R. Osher, H. Wang, K. Lee, Y. Zhang, Y. Huang, J. D. Finan, J. A. Rogers, *Sci. Adv.* **2021**, *7*, eabf9153.

[13] X. Yang, C. Forró, T. L. Li, Y. Miura, T. J. Zaluska, C.-T. Tsai, S. Kanton, J. P. McQueen, X. Chen, V. Mollo, F. Santoro, S. P. Paşca, B. Cui, *Nat. Biotechnol.* **2024**, https://doi.org/10.1038/s41587-023-02081-3.

[14] P. L. Floch, Q. Li, Z. Lin, S. Zhao, R. Liu, K. Tasnim, H. Jiang, J. Liu, *Adv. Mater.* **2022**, *34*, 2106829.

[15] M. McDonald, D. Sebinger, L. Brauns, L. Gonzalez-Cano, Y. Menuchin-Lasowski, M. Mierzejewski, O.-E. Psathaki, A. Stumpf, J. Wickham, T. Rauen, H. Schöler, P. D. Jones, *Biosens. Bioelectron.* **2023**, *228*, 115223.

[16] E. M. Maynard, C. T. Nordhausen, R. A. Normann, *Electroencephalography and Clinical Neurophysiol.* **1997**, *102*, 228.

[17] H. Steins, M. Mierzejewski, L. Brauns, A. Stumpf, A. Kohler, G. Heusel, A. Corna, T. Herrmann, P. D. Jones, G. Zeck, R. Von Metzen, T. Stieglitz, *Microsyst. Nanoeng.* **2022**, *8*, 131.

[18] J. Abu Shihada, M. Jung, S. Decke, L. Koschinski, S. Musall, V. Rincón Montes, A. Offenhäusser, *Adv. Sci.* **2024**, *11*, 2305944.

[19] P. Wijdenes, K. Haider, C. Gavrilovici, B. Gunning, M. D. Wolff, T. Lijnse, R. Armstrong, G. C. Teskey, J. M. Rho, C. Dalton, N. I. Syed, *Sci. Rep.* **2021**, *11*, 21952.

[20] J. Jiang, X. Chen, Z. Mei, H. Chen, J. Chen, X. Wang, S. Li, R. Zhang, G. Zheng, W. Li, *Micromachines* **2024**, *15*, 333.

[21] M. K. Saghafi, S. K. Vasantham, N. Hussain, G. Mathew, F. Colombo, B. Schamberger, E. Pohl, G. C. Marques, B. Breitung, M. Tanaka, M. Bastmeyer, C. Selhuber-Unkel, U. Schepers, M. Hirtz, J. Aghassi-Hagmann, *Adv. Funct. Mater.* **2024**, *34*, 2308613.

[22] M.d. A. Ali, C. Hu, E. A. Yttri, R. Panat, *Adv. Funct. Materials* **2022**, *32*, 2107671.

[23] M. Seiti, O. Degryse, R. Monica Ferraro, S. Giliani, V. Bloemen, E. Ferraris, *IJB* **2023**, *9*, 0257.

[24] M. Seiti, P. S. Ginestra, E. Ferraris, In *Selected Topics in Manufacturing*, (Eds.: L. Carrino, L. M. Galantucci, L. Settineri), Springer Nature, Switzerland, Cham, **2024**, pp. 19.

[25] M. S. Saleh, S. M. Ritchie, M. A. Nicholas, H. L. Gordon, C. Hu, S. Jahan, B. Yuan, R. Bezbaruah, J. W. Reddy, Z. Ahmed, M. Chamanzar, E. A. Yttri, R. P. Panat, *Sci. Adv.* **2022**, *8*, eabj4853.

[26] S. Zips, B. Huang, S. Hotte, L. Hiendlmeier, C. Wang, K. Rajamani, O. Buriez, G. Al Boustani, Y. Chen, B. Wolfrum, A. Yamada, *ACS Appl. Mater. Interfaces* **2023**, *15*, 35950.

[27] L. Grob, P. Rinklin, S. Zips, D. Mayer, S. Weidlich, K. Terkan, L. J. K. Weiß, N. Adly, A. Offenhäusser, B. Wolfrum, *Sensors* **2021**, *21*, 3981.

[28] M. Golda-Cepa, K. Engvall, M. Hakkarainen, A. Kotarba, *Prog. Org. Coat.* **2020**, *140*, 105493.

[29] H. Peng, L. Grob, L. J. K. Weiß, L. Hiendlmeier, E. Music, I. Kopic, T. F. Teshima, P. Rinklin, B. Wolfrum, *Nanoscale* **2023**, *15*, 4006.

[30] A. Haase, S. Rott, A. Mantion, P. Graf, J. Plendl, A. F. Thünemann, W. P. Meier, A. Taubert, A. Luch, G. Reiser, *Toxicol. Sci.* **2012**, *126*, 457.

[31] B. Bachmann, N. Y. Adly, J. Schnitker, A. Yakushenko, P. Rinklin, A. Offenhäusser, B. Wolfrum, *Flex. Print. Electron.* **2017**, *2*, 035003.

[32] L. J. K. Weiß, P. Rinklin, B. Thakur, E. Music, H. Url, I. Kopic, D. Hoven, M. Banzet, T. Von Trotha, D. Mayer, B. Wolfrum, *ACS Sens.* **2022**, *7*, 1967.

[33] X. Qian, F. Jacob, M. M. Song, H. N. Nguyen, H. Song, G. Ming, *Nat. Protoc.* **2018**, *13*, 565.

[34] S. R. Fair, D. Julian, A. M. Hartlaub, S. T. Pusuluri, G. Malik, T. L. Summerfied, G. Zhao, A. B. Hester, W. E. Ackerman, E. W. Hollingsworth, M. Ali, C. A. McElroy, I. A. Buhimschi, J. Imitola, N. L. Maitre, T. A. Bedrosian, M. E. Hester, *Stem Cell Rep.* **2020**, *15*, 855.

[35] X. Qian, H. Song, G. Ming, *Development* **2019**, *146*, dev166074.

[36] S. Schmidt, C. Stautner, D. T. Vu, A. Heinz, M. Regensburger, O. Karayel, D. Trümbach, A. Artati, S. Kaltenhäuser, M. Z. Nassef, S. Hembach, L. Steinert, B. Winner, W. Jürgen, M. Jastroch, M. D. Luecken, F. J. Theis, G. G. Westmeyer, J. Adamski, M. Mann, K. Hiller, F. Giesert, D. M. Vogt Weisenhorn, W. Wurst, *Nat. Commun.* **2023**, *14*, 7674.